



Defense Threat Reduction Agency
8725 John J. Kingman Road, MS-6201
Fort Belvoir, VA 22060-6201



DTRA-TR-14-46

TECHNICAL REPORT

Multimillion Atom Simulations of Nanoenergetic Materials

Distribution Statement A. Approved for public release; distribution is unlimited.

December 2014

HDTRA1-07-1-0023

Priya Vashishta et al.

Prepared by:
Collaboratory for Advanced
Computing and Simulations
Department of Computer
Sciences
University of Southern California
3651 Watt Way, VHE 608
Los Angeles, CA 90089

DESTRUCTION NOTICE:

Destroy this report when it is no longer needed.
Do not return to sender.

PLEASE NOTIFY THE DEFENSE THREAT REDUCTION
AGENCY, ATTN: DTRIAC/ J9STT, 8725 JOHN J. KINGMAN ROAD,
MS-6201, FT BELVOIR, VA 22060-6201, IF YOUR ADDRESS
IS INCORRECT, IF YOU WISH THAT IT BE DELETED FROM THE
DISTRIBUTION LIST, OR IF THE ADDRESSEE IS NO
LONGER EMPLOYED BY YOUR ORGANIZATION.

REPORT DOCUMENTATION PAGE			<i>Form Approved</i> OMB No. 0704-0188	
Public reporting burden for this collection of information is estimated to average 1 hour per response, including the time for reviewing instructions, searching existing data sources, gathering and maintaining the data needed, and completing and reviewing this collection of information. Send comments regarding this burden estimate or any other aspect of this collection of information, including suggestions for reducing this burden to Department of Defense, Washington Headquarters Services, Directorate for Information Operations and Reports (0704-0188), 1215 Jefferson Davis Highway, Suite 1204, Arlington, VA 22202-4302. Respondents should be aware that notwithstanding any other provision of law, no person shall be subject to any penalty for failing to comply with a collection of information if it does not display a currently valid OMB control number. PLEASE DO NOT RETURN YOUR FORM TO THE ABOVE ADDRESS.				
1. REPORT DATE (DD-MM-YYYY) 00-12-2014		2. REPORT TYPE Technical		3. DATES COVERED (From - To) December 2006 - December 2009
4. TITLE AND SUBTITLE Multimillion Atom Simulations of Nanoenergetic Materials			5a. CONTRACT NUMBER HDTRA1-07-1-0023	
			5b. GRANT NUMBER	
			5c. PROGRAM ELEMENT NUMBER	
6. AUTHOR(S) Priya Vashishta Rajiv K. Kalia Aiichiro Nakano			5d. PROJECT NUMBER	
			5e. TASK NUMBER	
			5f. WORK UNIT NUMBER	
7. PERFORMING ORGANIZATION NAME(S) AND ADDRESS(ES) Collaboratory for Advanced Computing and Simulations Department of Computer Sciences University of Southern California 3651 Watt Way, VHE 608 Los Angeles, CA 90089			8. PERFORMING ORGANIZATION REPORT NUMBER	
9. SPONSORING / MONITORING AGENCY NAME(S) AND ADDRESS(ES) Defense Threat Reduction Agency 8725 John J. Kingman Road STOP 6201 Fort Belvoir, VA 22060 PM/Suhithi Peiris			10. SPONSOR/MONITOR'S ACRONYM(S) DTRA	
			11. SPONSOR/MONITOR'S REPORT NUMBER(S) DTRA-TR-14-46	
12. DISTRIBUTION / AVAILABILITY STATEMENT Distribution Statement A. Approved for public release; distribution is unlimited.				
13. SUPPLEMENTARY NOTES				
14. ABSTRACT This final product describes the work performed at USC in fulfillment of a research project for DTRA. The objective is to perform first-principles based and experimentally validated, atomistic simulations of reactive nanosystems involving multi million atoms to achieve atomistic-level understanding and predictive power for designing advanced and insensitive nanostructured energetic materials. The study will focus on reactive and mechanical behavior of Al nanoparticles as well as thermo-mechanical properties and atomistic mechanisms of detonation of nanostructured materials consisting of Al nanoparticles encapsulated in nanophase RDX and oxidizers.				
15. SUBJECT TERMS Quantum mechanical (QM); Molecular dynamics (MD); Simulation framework, Aluminum nanoparticles				
16. SECURITY CLASSIFICATION OF:			17. LIMITATION OF ABSTRACT UU	18. NUMBER OF PAGES 32
a. REPORT Unclassified	b. ABSTRACT Unclassified	c. THIS PAGE Unclassified		
				19b. TELEPHONE NUMBER (include area code) 703-767-4732

CONVERSION TABLE

Conversion Factors for U.S. Customary to metric (SI) units of measurement.

MULTIPLY → BY → TO GET
TO GET ← BY ← DIVIDE

angstrom	1.000 000 x E -10	meters (m)
atmosphere (normal)	1.013 25 x E +2	kilo pascal (kPa)
bar	1.000 000 x E +2	kilo pascal (kPa)
barn	1.000 000 x E -28	meter ² (m ²)
British thermal unit (thermochemical)	1.054 350 x E +3	joule (J)
calorie (thermochemical)	4.184 000	joule (J)
cal (thermochemical/cm ²)	4.184 000 x E -2	mega joule/m ² (MJ/m ²)
curie	3.700 000 x E +1	*giga bacquerel (GBq)
degree (angle)	1.745 329 x E -2	radian (rad)
degree Fahrenheit	$t_k = (t^{\circ}f + 459.67)/1.8$	degree kelvin (K)
electron volt	1.602 19 x E -19	joule (J)
erg	1.000 000 x E -7	joule (J)
erg/second	1.000 000 x E -7	watt (W)
foot	3.048 000 x E -1	meter (m)
foot-pound-force	1.355 818	joule (J)
gallon (U.S. liquid)	3.785 412 x E -3	meter ³ (m ³)
inch	2.540 000 x E -2	meter (m)
jerk	1.000 000 x E +9	joule (J)
joule/kilogram (J/kg) radiation dose absorbed	1.000 000	Gray (Gy)
kilotons	4.183	terajoules
kip (1000 lbf)	4.448 222 x E +3	newton (N)
kip/inch ² (ksi)	6.894 757 x E +3	kilo pascal (kPa)
ktap	1.000 000 x E +2	newton-second/m ² (N-s/m ²)
micron	1.000 000 x E -6	meter (m)
mil	2.540 000 x E -5	meter (m)
mile (international)	1.609 344 x E +3	meter (m)
ounce	2.834 952 x E -2	kilogram (kg)
pound-force (lbs avoirdupois)	4.448 222	newton (N)
pound-force inch	1.129 848 x E -1	newton-meter (N-m)
pound-force/inch	1.751 268 x E +2	newton/meter (N/m)
pound-force/foot ²	4.788 026 x E -2	kilo pascal (kPa)
pound-force/inch ² (psi)	6.894 757	kilo pascal (kPa)
pound-mass (lbm avoirdupois)	4.535 924 x E -1	kilogram (kg)
pound-mass-foot ² (moment of inertia)	4.214 011 x E -2	kilogram-meter ² (kg-m ²)
pound-mass/foot ³	1.601 846 x E +1	kilogram-meter ³ (kg/m ³)
rad (radiation dose absorbed)	1.000 000 x E -2	**Gray (Gy)
roentgen	2.579 760 x E -4	coulomb/kilogram (C/kg)
shake	1.000 000 x E -8	second (s)
slug	1.459 390 x E +1	kilogram (kg)
torr (mm Hg, 0° C)	1.333 22 x E -1	kilo pascal (kPa)

*The bacquerel (Bq) is the SI unit of radioactivity; 1 Bq = 1 event/s.

**The Gray (GY) is the SI unit of absorbed radiation.

Final Technical Report (December 18, 2006—December 17, 2009)

Defense Threat Reduction Agency Grant # HDTRA1-07-1-0023

Multimillion Atom Simulations of Nanoenergetic Materials

Priya Vashishta, Rajiv K. Kalia, and Aiichiro Nakano

Collaboratory for Advanced Computing and Simulations

Departments of Chemical Engineering & Materials Science, Physics & Astronomy, and

Department of Computer Science

University of Southern California

3651 Watt Way, VHE 608, Los Angeles, CA 90089-0242

Email: (priyav, rkalia, anakano)@usc.edu

Phone: (213) 821-2662; Fax: (213) 821-2664

Objectives:

To perform first-principles based and experimentally validated, atomistic simulations of reactive nanosystems involving multimillion atoms to achieve atomistic-level understanding and predictive power for designing advanced and insensitive nanostructured energetic materials, so that safety and survivability will be increased with enhanced performance. We study:

- ***Reactive and mechanical behavior of aluminum nanoparticles.*** We determine the stability, energetics, and mechanical properties of aluminum particles coated with oxide shells to understand their structures, adhesion, size effects, and mechanical stability under shock and flash heating.
- ***Thermo-mechanical properties and atomistic mechanisms of detonation of nanostructured materials consisting of Al nanoparticles encapsulated in nanophase RDX and oxidizers.*** We investigate shock- and thermally-induced initiation of detonation, chemically sustained shock waves, and shock-induced flow initiation at the interfaces, with the goal of determining the role of crystal morphology and defects (such as voids, dislocations, and grain boundaries) and predicting material properties prior to their experimental synthesis.

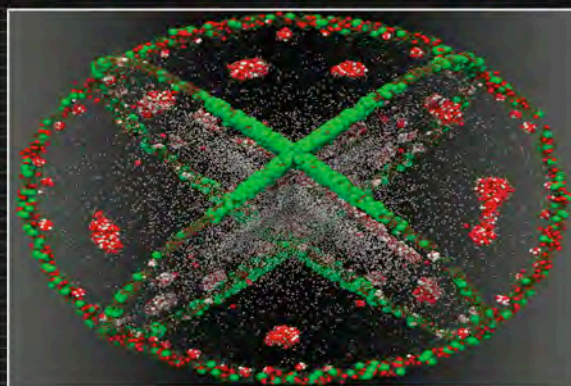
Approach:

We use our adaptive hierarchical quantum mechanical (QM)/molecular dynamics (MD) simulation framework, which invokes higher accuracy simulations only when and where high fidelity is required. We have developed scalable parallel QM and MD simulation algorithms, with which we have benchmarked unprecedented scales of quantum-mechanically accurate and well validated, chemically reactive atomistic simulations—1.72 billion-atom reactive MD and 1.68 trillion electronic degrees-of-freedom (19.2 million-atom) QM simulation in the framework of the density functional theory—in addition to 218 billion-atom non-reactive MD, with parallel efficiency well over 0.95 on 212,992 CPUs. We also perform multimillion-to-multibillion atom MD simulations in house at USC on our 2,048-CPU Opteron cluster.

Highlight:

Our multimillion-atom molecular-dynamics simulation supported under this project revealed fast reaction mechanisms of a core (Al)-shell (Al_2O_3) nanoparticle in oxygen, and was featured on the cover of *Applied Physics Letters* (28 December 2009 issue, see below).

APPLIED PHYSICS LETTERS



0003-6951(20091228)95:26;1-A

AMERICAN
INSTITUTE
OF PHYSICS

APPLIED PHYSICS LETTERS 95, 261901 (2009)

Fast reaction mechanism of a core(Al)-shell (Al_2O_3) nanoparticle in oxygen

Weiqliang Wang, Richard Clark, Aiichiro Nakano, Rajiv K. Kalia, and Priya Vashishta^{a)}
*Collaboratory for Advanced Computing and Simulations, Department of Physics and Astronomy,
Department of Chemical Engineering and Materials Science, and Department of Computer Science,
University of Southern California, Los Angeles, California 90089-0242, USA*

(Received 30 July 2009; accepted 3 November 2009; published online 28 December 2009)

Atomistic mechanisms of oxidation in a laser flash heated core (Aluminum)-shell (Alumina) nanoparticle are investigated using multimillion-atom molecular dynamics simulations. We find a thermal-to-mechanochemical transition of oxidation mechanism when the initial core temperature is above 6000 K. The transition from thermal diffusion to mechanically enhanced diffusion to ballistic transport is accompanied by a change in the intermediate reaction products from Al rich Al_2O to oxygen rich AlO_2 clusters. Higher initial temperature of the core causes catastrophic failure of the shell, which provides direct oxidation pathways for core Al, resulting in faster energy release.
© 2009 American Institute of Physics. [doi:10.1063/1.3268436]

This work was supported by the Basic Research Program of Defense Threat Reduction Agency. Simulations were performed at the CACS and HPC center at USC. We thank Dr. Suhithi Peiris for stimulating discussions.

Status of Efforts:

Fundamental understanding and precise control of reaction rates and initiation time are of critical importance for nanostructured energetic materials. However, the reactivity of nanoenergetic materials is known to differ drastically from their micron-scale counterparts. For example, experimental studies on the combustion of nanothermites, such as $\text{Al}/\text{Fe}_2\text{O}_3$ and Al/MoO_3 , have shown that flame propagation speeds approach km/s when the size of Al nanoparticles is reduced to below 100 nm, in contrast to cm/s for traditional thermites. Another example is the two-stage reaction of Al/CuO -nanowire thermite, in which the first reaction takes place at 500 °C followed by the second reaction at 660 °C (i.e., Al melting temperature). Such peculiar reactive behaviors of nanothermites cannot be explained by conventional mechanisms based on mass diffusion of reactants, and thus various alternative mechanisms have been proposed. An example is a mechanochemical mechanism that explains the fast flame propagation based on dispersion of the molten metal core of each nanoparticle and spallation of the oxide shell covering the metal core. Another mechanism is accelerated mass transport of both oxygen and metal atoms due to the large pressure gradient between the metal core and the oxide shell of each metal nanoparticle. In addition, defect-mediated giant diffusivity is important for fast reactions at the nanometer scale.

To explain the observed fast reactivity of various MICs (e.g. $\text{Al}+\text{MoO}_3$ and $\text{Al}+\text{Fe}_2\text{O}_3$ nanocomposites), a melt-dispersion mechanism has been proposed by considering the spallation of the oxide shell due to the high pressure of the molten metal core when the nanoparticle is heated. In laser flash-heating experiments of ALEX by Dlott's group, a linear relationship was found between the reaction propagation distance and laser energy, which was explained with a hydrodynamic model instead of the thermal explosion model. However, no single theory explains all observed behaviors of nanoparticle combustion. As mentioned above, mechanical breakdown of the nanoparticle's shell has been suggested to play an important role in the initiation of MIC, but atomistic processes underlying this mechanism are yet to be understood.

We have performed multimillion-atom reactive MD simulations to study atomistic mechanisms of the oxidation of a core (aluminum)-shell (alumina) nanoparticle (ANP). We have found a thermal-to-mechanochemical transition of oxidation mechanism at elevated temperatures. The transition from thermal diffusion to mechanically enhanced diffusion to ballistic transport of atoms is accompanied by a change of intermediate reaction products from aluminum-rich to oxygen-rich clusters. Higher initial temperature of the Al core causes catastrophic fracture of the alumina shell during the expansion of the ANP, which provides direct oxidation pathways for core Al atoms, resulting in faster oxidation reaction and thus faster energy release.

Our multimillion-atom MD simulations also reveal significant effects of the structure of oxide shells on the burning behavior of an ANP. With a crystalline shell, radial expansion of the nanoparticle followed by its contraction forms pores in the shell, resulting in enhanced oxidation reactions. With an amorphous shell, formation of oxide nanoclusters by the shattering of the shell, combined with the fragmentation and dispersion of the nanoparticle, catalyzes oxidation reactions that would otherwise take much longer times. Consequently, the energy release rate of an ANP with an amorphous shell is much larger than that with a crystalline shell. Fragment analysis on the formation of oxygen-rich fragments further confirms an enhanced reaction rate with an amorphous shell.

The above simulations have shown the transition of reaction mechanisms, but at elevated temperatures. Because the onset or ignition temperatures of thermites are often considered as a function of the heating rate, it is also of great interest for us to carry out the study on the reaction of the ANP using different heating rates. We have thus performed multimillion-atom MD simulations of slower burning ANPs in oxygen and found the onset temperature (~ 740 °C) at which self-heating begins. The simulation results reveal a three-stage reaction mechanism involving confined and spallation phases. Initiation is focused in hot spot areas, which develop at the inner boundary of alumina shell and aluminum core. Resulting increase in oxygen mobility provides energetically favorable migration of oxygen into aluminum core. The oxygen diffusion at the internal boundary is the primary mechanism of energy release in the first reaction phase, leading to local temperature extremes along the shell.

Simulation results show a transition to a second reaction mechanism when the local temperature of the alumina shell exceeds the melting point of alumina. Localized heating at the shell and development of oxygen-poor regions lead to shell shape deformation and an increase in oxygen absorption from the environment. Resulting shell failure leads to the third stage of spallation of small aluminum clusters into surrounding oxygen, generating additional heat by direct oxidation. Mechanism of reaction in the three stages and identification of transition point are confirmed via fragment analysis, radial composition/temperature analysis, and statistical particle migration calculations.

In experiments and real applications of nanoscale composite energetic materials, the mixture powder can often contain millions of the additive fuel—the aluminum nanoparticles. Heating schedule for these aluminum nanoparticles can be very different due to their accessibility to the heat source. Aluminum nanoparticles exposed earlier to the heat source thus will react first, which can release large amount of and ignite the neighboring nanoparticles that are not exposed to the initial heat source, resulting in the self-sustained detonation till all the fuels are consumed. In experiments, it has been found that the flame velocity of the nanoscale energetic composites can reach up to 1000 m/s, and the convective flow is predicted to be the dominant mechanism that accounts for the fast heat transport. In order to see the synergetic reactions of multiple aluminum nanoparticles induced by a portion of preheated ones, we have performed multi-million atom MD studies on the reaction of a linear chain of three aluminum nanoparticles.

This study of induced oxidation reaction of an ANP due to the ignition of neighboring ANPs on a linear chain has revealed the mode and effect of heat transfer from outer ANPs to a central ANP. Our MD study has confirmed the experimentalists proposed heat transfer mode of convection i.e. flow of hot atoms from one ANP to the other. Such a flow begins only after the neighboring hot ANPs reach their final stage of burning. Different reaction dynamics are found for the preheated outer ANPs from the center one, reaction of which is induced by the ignition of outer ANPs. We found the central ANP undergoes two stages of burning as opposed to three stages observed in the outer ANPs. While the outer ANPs burn completely by 700 ps, the central ANP begins to burn only after 300 ps when the outer ANPs start to penetrate into it from the zones of contact. Ejection of pure Aluminum atoms from the core into the outside environment was observed in both outer and central ANPs, though at different times during the simulations. The onset of ejections coincided with the beginning of the last stage of burning in the respective ANP. Apart from heating the central ANP, the hot atoms from outer ANPs also initiate exothermic thermite reactions inside the central ANP, which releases energy, further heating the central ANP. By 1 ns, all the three ANPs fuse together to form one single aggregate. From the

above observations, it can be concluded that a hot ANP can heat up and detonate a closely spaced neighboring ANP by penetrating into it and also initiating thermite reactions, both of which would lead to the eventual detonation of the neighboring ANP.

We have also performed divide-and-conquer density functional theory (DC-DFT) based MD simulations to study thermite reaction at an Al/Fe₂O₃ interface. The results reveal a concerted metal-oxygen flip mechanism that significantly enhances the rate of redox reactions. This mechanism leads to two-stage reactions—rapid initial reaction due to collective metal-oxygen flips followed by slower reaction based on uncorrelated diffusive motions, which may explain recent experimental observation in thermite nanowire arrays mentioned above. The 1,152-atom DC-DFT MD simulation for 5 ps (6000 MD time steps) took 985 hours on 960 (3.2 GHz Intel Xeon) processors.

Accomplishments/New Findings:

Flash Heating of an Aluminum Nanoparticle—Temperature Dependence

We have performed molecular-dynamics (MD) simulations to study the flash heating of a single 48 nm aluminum nanoparticle (ANP), which has a 4 nm alumina shell, and the ANP is embedded in oxygen. A total of 11,018,467 atoms—including 1,928,931 core Al, shell atoms (1,152,528 Al and 1,727,292 O), and 6,210,716 environmental oxygen surrounding the nanoparticle—are contained in a cubic box with edge length of 226.419 nm, see Fig. 1(a).

In laser flash-heating experiments of ALEX by Dlott et al., the wavelength of laser beam is selected in the near IR regime ($\sim 1.06 \mu\text{m}$), which is absorbed only by the metal core leaving the oxide shell unheated. Similarly, at the start of our simulations, the Al core is heated, while the shell is maintained at room temperature. To study the effect of the initial core temperature, we heat the core of the ANP to 3000, 6000 and 9000 K, which will be referred to as C3, C6 and C9 systems, respectively. These systems are then thermalized for 2 ps while keeping the alumina shell atoms fixed. To obtain a uniformly heated core, Langevin dynamics is run at the desired temperature for the core atoms for an additional picosecond. After this preparation, the constraints on the shell atoms are removed and the nanoparticle undergoes thermal expansion for 200 ps within the microcanonical ensemble.

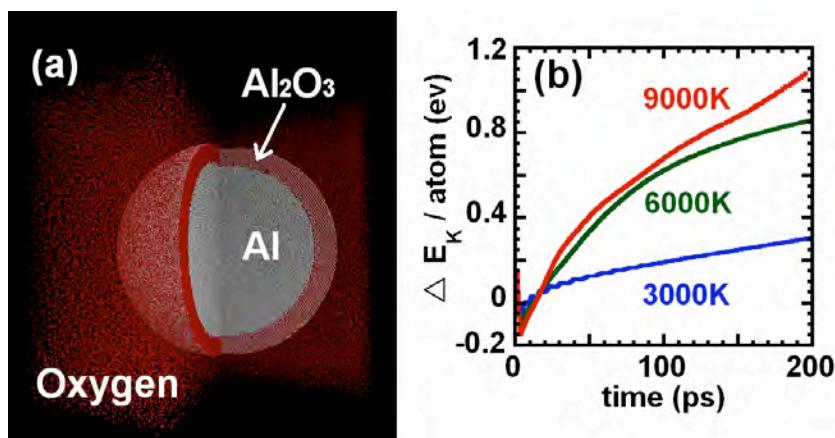


Fig. 1: (a) Initial setup of the system consisting of a single core-shell nanoparticle embedded in oxygen. Most of the oxygen atoms surrounding the nanoparticle are not shown for clarity. To show the inside, a quarter of the nanoparticle has been removed. (b) Increase of kinetic energy per Al atom in the process of oxidation for the C3 (3000K), C6 (6000K) and C9 (9000K) systems.

To compare the different energy release rates in the three systems, time variation of the average kinetic energy per atom is shown in Fig. 1(b). We observe that among the three systems, higher initial core temperature releases more energy up to 200 ps. This correspondence between higher initial heat in the Al core and faster reaction of the nanoparticle is consistent with experiments by Dlott et al. In their experiments, the energy release rate was inferred from the consumption rate of oxidizers by ALEX fuel. They also found that the energy release is a two-stage process, consisting of initial reaction of Al fuel with the surrounding oxidizer and subsequent slower consumption of oxidizer in between Al nanoparticles. Our simulation results in Fig. 1(b) reveal similar two-stage energy release characteristics. In all three systems, after the initial rapid drop of the kinetic energy due to the expansion of the shell, the kinetic energy of each atom increases rapidly at first and at a slower rate subsequently. Figure 1(b) also shows that the energy release rate for the C3 system is much lower. The energy release rates of C6 and C9 are similar in the first 100 ps, but subsequently it slows down for C6 whereas it continues to increase in C9.

The fastest energy release is seen for the C9 system (see Fig. 1(b)). Here, detailed analysis of the atom migration events reveals a novel mechanism involving ballistic transport of atoms resulting from the opening of pores in the shell (see Fig. 2(c)). Calculation of shell's minimum thickness shows that pores in the shell appear as early as at 22 ps. This catastrophic mechanical breakdown of the shell removes the protective layer that would prevent further oxidation of the core Al atoms. The opening of pathways for oxidation ensures more complete oxidation of the nanoparticle over time, and thus much more energy is released in the C9 system than in C6. This is consistent with the energy-release plot in Fig. 1(b).

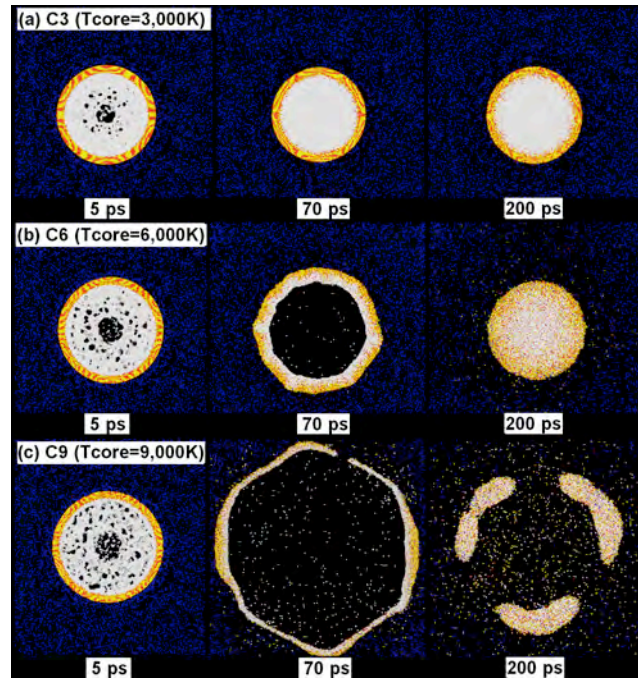


Fig. 2: Snapshots of the nanoparticle at different times with initial core temperature of (a) 3000K, (b) 6000K, and (c) 9000K. The core aluminum is shown as white; shell aluminum, yellow; shell oxygen, red; and environmental oxygen, blue.

Figure 3(a) is a semi-log plot of the number of core Al atoms jetting into the oxygen environment. The C3 system shows no direct transport of core Al to oxygen environment

because of the intact shell surrounding the core. For C6, the number of core Al atoms that cross the shell is on the order of hundred, signifying limited direct oxidation reactions between core Al and oxygen. This number is small because the expansion of the shell driven by the pressure of the core is not large enough to generate pores in the shell. Instead, there are low-density regions in the shell (Fig. 3(b)), through which core Al jet out (Fig. 3(c)). These low-density regions close up again in the subsequent shrinking phase and prohibit further jetting out of core Al into the environment. In C9, the number of core Al that jet into oxygen environment is orders-of-magnitude larger than that in C6 (Fig. 3(a)) due to the opening of large pores in the shell (Fig. 3(d)) that provides pathways for the core Al to directly pass through the shell (Fig. 3(e)). The large number of ballistically transported core Al into the environment results in the fastest energy release rate for C9, and permanent opening of pores in the shell of C9 ensures continuous oxidation of the core Al even after 100 ps (Fig. 1(b)).

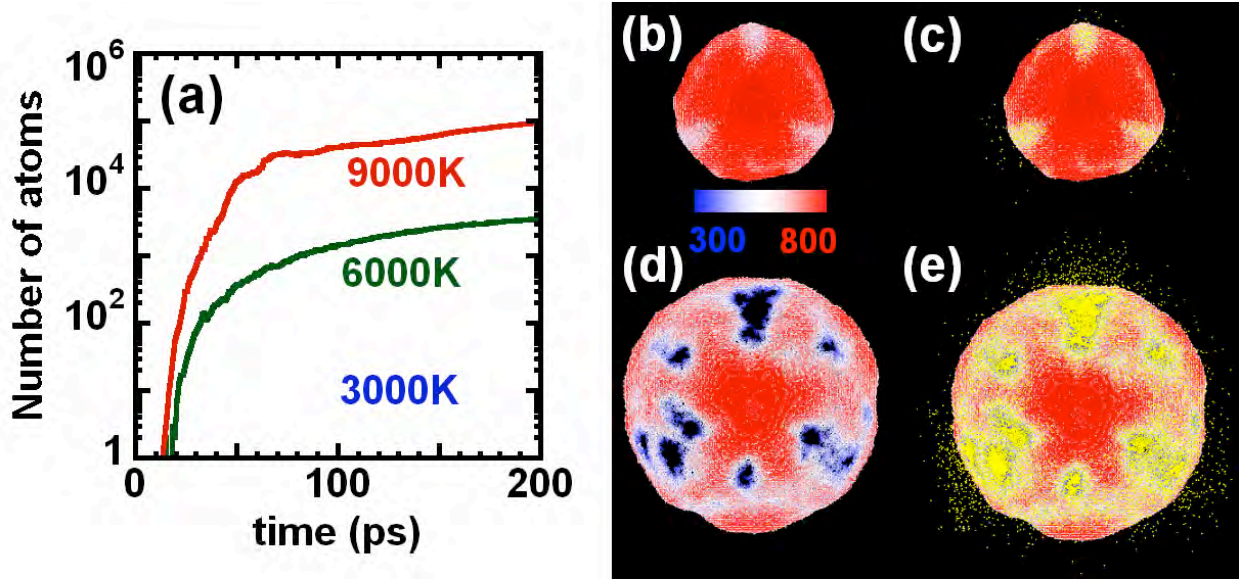


Fig. 3: (a) Semi-log plot of the number of Al core atoms jetting into oxygen environment in the C3, C6 and C9 systems. (b) and (d) are snapshots of shell morphology in C6 and C9, respectively, at 100ps with colors representing the number density (in unit of number of atoms/nm³) in the shell as shown by the color bar. (c) and (e) are snapshots of the shell morphology superimposed with jetting-out core aluminum atoms (in yellow) for C6 and C9, respectively. Environmental oxygen is not shown for clarity of presentation.

Experimentally, the burning of an Al nanoparticle has been found to last several nanoseconds before the most stable products Al₂O₃ are formed. Simulations of the oxidation of Al clusters and experiments of the laser ablation of Al films have all shown the production of AlO before the formation of the final product Al₂O₃. During our simulations, as expected, many intermediate reaction products are observed. We have investigated the size distribution and chemical composition of the oxide fragments in the three systems. The majority of fragments in all three systems are small having less than 6 atoms, while the number of fragments is larger for higher initial core temperatures. In all three systems, there is only one fragment having the number of atoms larger than 1000, which is the shell consisting of 2,978,188, 3,156,289 and 3,544,013 atoms for C3, C6 and C9, respectively. Table I shows the statistics and chemical composition of fragments in C3, C6 and C9 at 200 ps. In C3, the majority of small fragments are Al₂O, all inside the nanoparticle near the interface of the shell and the core. In C6, AlO are the major fragments, and oxygen-rich fragments are also present outside the nanoparticle. Oxygen-rich AlO₂

fragments are dominant in C9. In experiments, intermediate aluminum oxides with various composition ratios have been observed, where AlO and AlO₂ are two major products. In our simulations, the number of fragments increases with higher core temperatures, and the chemical composition of major fragments changes from Al-rich to O-rich, indicating the increased rate of oxidation.

Table I: Statistics and chemical composition of fragments in C3, C6 and C9 systems at 200 ps.

	Al ₄ O	Al ₃ O	Al ₂ O	AlO	Al ₂ O ₃	AlO ₂
C3	3,235	6,508	7,998	5,332	81	29
C6	1,706	6,343	15,209	24,894	1,658	14,200
C9	126	655	6,107	98,828	3,185	113,796

We have thus found a fast reaction mechanism in which the opening of pores in the oxide shell at higher core temperatures lead to faster and more complete oxidation of nanoparticles, resulting in higher energy release rates. Catastrophic fracture of the shell enhances the oxidation process by weakening or destroying the protective shell of the ANP, thereby providing pathways for ballistic transport of atoms. Faster oxidation at higher temperatures is evidenced by the production of more oxygen-rich molecular fragments at earlier times. The effect of the core temperature on the oxidation process and the energy release rate in our simulations is consistent with Dlott's experiments. Experiments by Zachariah's group have confirmed the formation of hollow ANP after the oxidation at elevated temperatures.

Flash Heating of an Aluminum Nanoparticle—Effects of Oxide Shell Structures

In the study described above, we have treated the oxide shell of the ANP as a single crystal (α -Al₂O₃) for simplicity. However, experimental observations by Ramaswamy et al. and Gertsman and Kwok have both suggested that the structure of the alumina shell of ANPs is likely to be amorphous with partial crystalline regions. In experiments on the oxidation of ANPs, the crystallization of the amorphous shell has also been observed. As such, the effect of oxide-shell structures must be understood for the study of the burning of ANP.

To study the effect of the shell structure, we have performed multimillion-atom MD simulations of the burning of an ANP covered with either a crystalline or an amorphous alumina shell, which will be referred to CS and AS systems, respectively. The burning takes place in an oxygen environment, and for each system the Al core of the ANP is heated to the highest temperature used in the previous study.

To determine the effect of the shell structure on the reactivity of the ANP, we measure the energy release rate for both systems by plotting the increase in average kinetic energy per atom as a function of time in Fig. 4. It is seen that a significant amount of extra heat is produced with the amorphous shell as compared to the crystalline shell, indicating a greatly enhanced reaction rate of the ANP due to the change of the shell structure.

In order to understand the considerable difference in reaction rate due to the different shell structures in Fig. 4, we next examine the expansion behavior of the two systems in Fig. 5. Figure 5(a) plots the outer radius of the ANP, in which the AS system exhibits continuous expansion. In contrast, the CS system shows expansion followed by shrinkage. The radius is calculated as the average distance of all atoms contained within the large oxide fragments (those having over a thousand atoms) to the center of the system. Figures 5(c) and (d) show snapshots of the center

slice of the CS and AS systems at 70 and 200 ps, respectively. In the 3D view, the segments of the shell in the CS system in Fig. 5(c) are indeed connected and are part of the largest oxide fragment in the system (i.e. the shell with pores). However, in the AS system, the fragments shown in Fig. 5(d) are disconnected, indicative of multiple shattered pieces of the shell. This shattering of the shell can also be seen quantitatively by comparing the percentage of atoms in the largest oxide fragment at a given time to that at the beginning of the simulation, see Fig. 5(b). At 0 ps, the largest oxide fragment is the shell in both systems. Fig. 5(b) shows that the number of the atoms in the shell in the CS system increases continuously due to oxidation reactions on the shell surface, but it decreases by several orders of magnitude in the AS system, indicating that the shell is breaking apart. Continuous oxidation of the shell in the CS system (Fig. 5(c)) protects the Al core it encloses from oxidation, resulting in the slower reaction rate in the CS system. On the other hand, all the fragments in the AS system are small (Fig 5(d)). Aluminum atoms in these fragments are mostly under-coordinated and prone to further oxidation. This partially accounts for the faster energy release rate of the AS seen in Fig. 4.

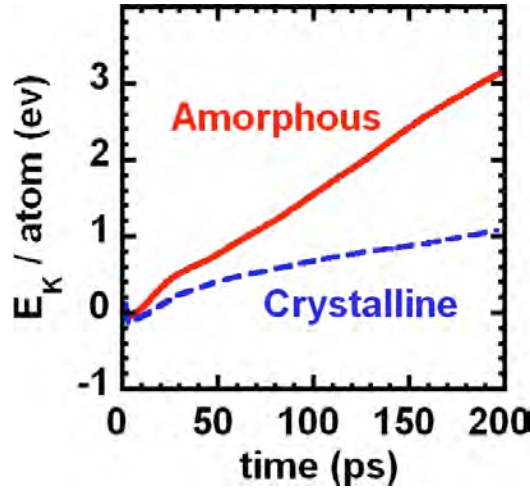


Fig. 4: Increase in the average kinetic energy per atom during combustion as a function of time for both crystalline and amorphous shells.

The other factor responsible for the faster energy release rate in the AS is the increased amount of core Al atoms which are dispersed into the surrounding oxygen and able to be directly oxidized by the environmental oxygen, as seen in Fig. 6. Figs. 6(a) and (c) show the projected view of the CS and AS shells, respectively, at 100 ps with the color indicating the local number density within the shell. Figures 6(b) and (d) show the core Al atoms (colored yellow) jetting out of the CS and AS shells, respectively. In both systems, there are many core Al atoms jetting out, causing direct, and thus faster, oxidation reactions. But spatial symmetries of the crystalline structure result in symmetric pores in the corresponding shell (see Fig. 6(a)). In contrast, the formation of pores occurs randomly in the amorphous shell (Fig. 6(c)). The opening of pores in the crystalline shell results in less overall area for the core Al atoms to move through. This is seen quantitatively from Figs. 6(e) and (f). Figure 6(e) plots the areal percentage of the pores of the shell, whereas Fig. 6(f) plots the number of core Al atoms that jet out. We see that the amorphous shell has a much larger area corresponding to pores. As a result, far more core Al atoms jet out in the AS system, resulting in more direct oxidations in the surrounding region and a faster heat release. This is consistent with the energy release rate curves in Fig. 4.

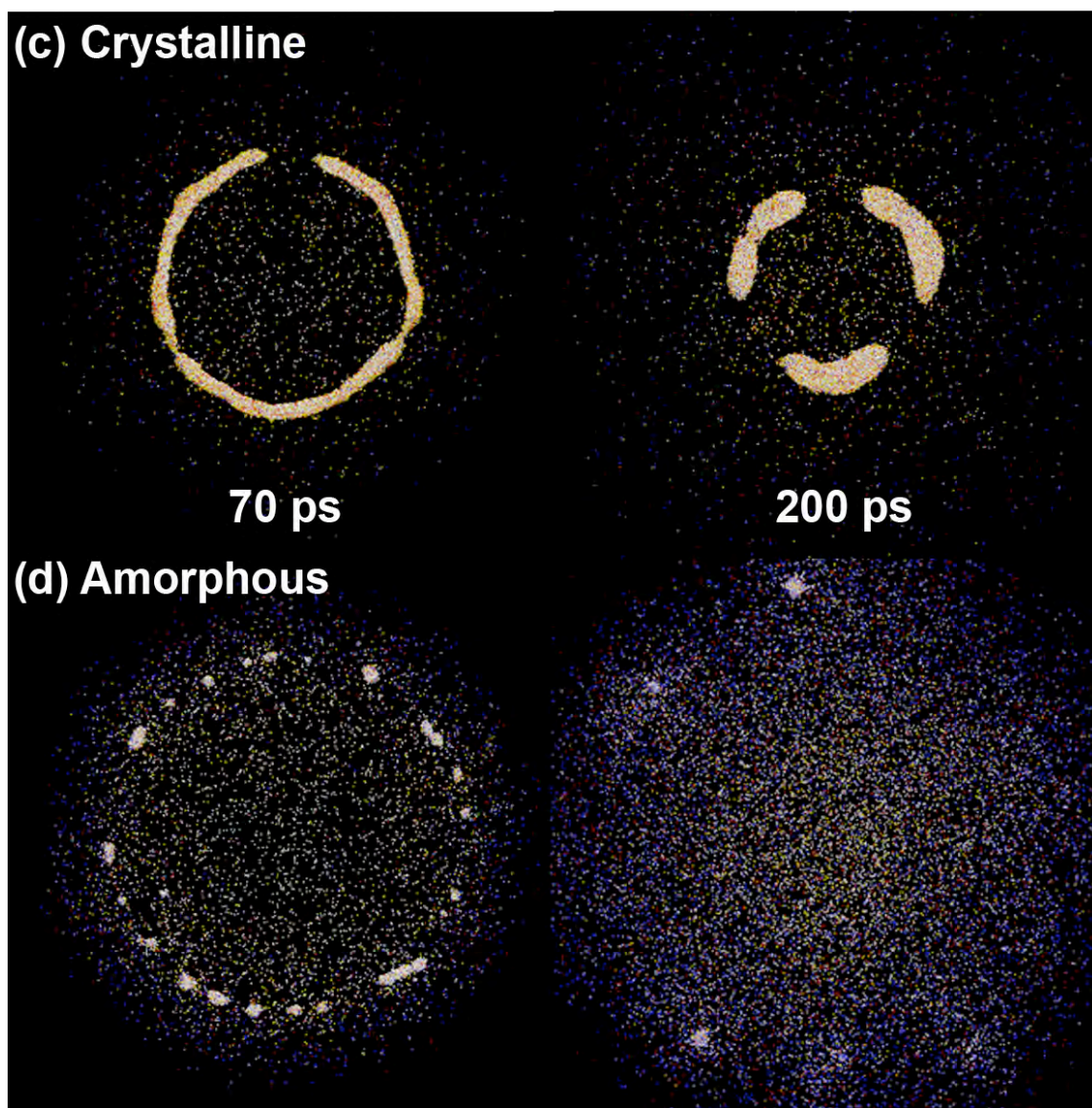


Fig. 5: The different expansion behavior of CS and AS systems are illustrated by (a) the radius of the ANP and (b) the percentage of atoms within the largest oxide fragment as a function of time. (c) and (d) show snapshots (at 70 and 200 ps) of the center slice of CS and AS systems, respectively, with atoms color coded by their species. The white color represents the Al core atoms; yellow, Al shell atoms; red, shell oxygen; and blue, the environmental oxygen. Environmental oxygen that is not covalently bonded to any Al atom is not shown for clarity of presentation.

We have thus found that an ANP covered with amorphous oxide-shell has much higher reactivity than that with crystalline shell. The crystalline shell expands and then shrinks, resulting in pore opening and the ejection of core Al atoms into the surrounding oxygen where fast oxidation occurs. In the crystalline system, though, there is a considerable amount of core aluminum that remains covered by the shell. In contrast, an ANP with amorphous shell continuously expands and shatters, resulting in only small oxide fragments and Al clusters which are prone to oxidation. The shattering of the amorphous shell also results in a larger area of the shell opening into pores, resulting in a much faster and widespread oxidation of the core Al atoms that jet out.

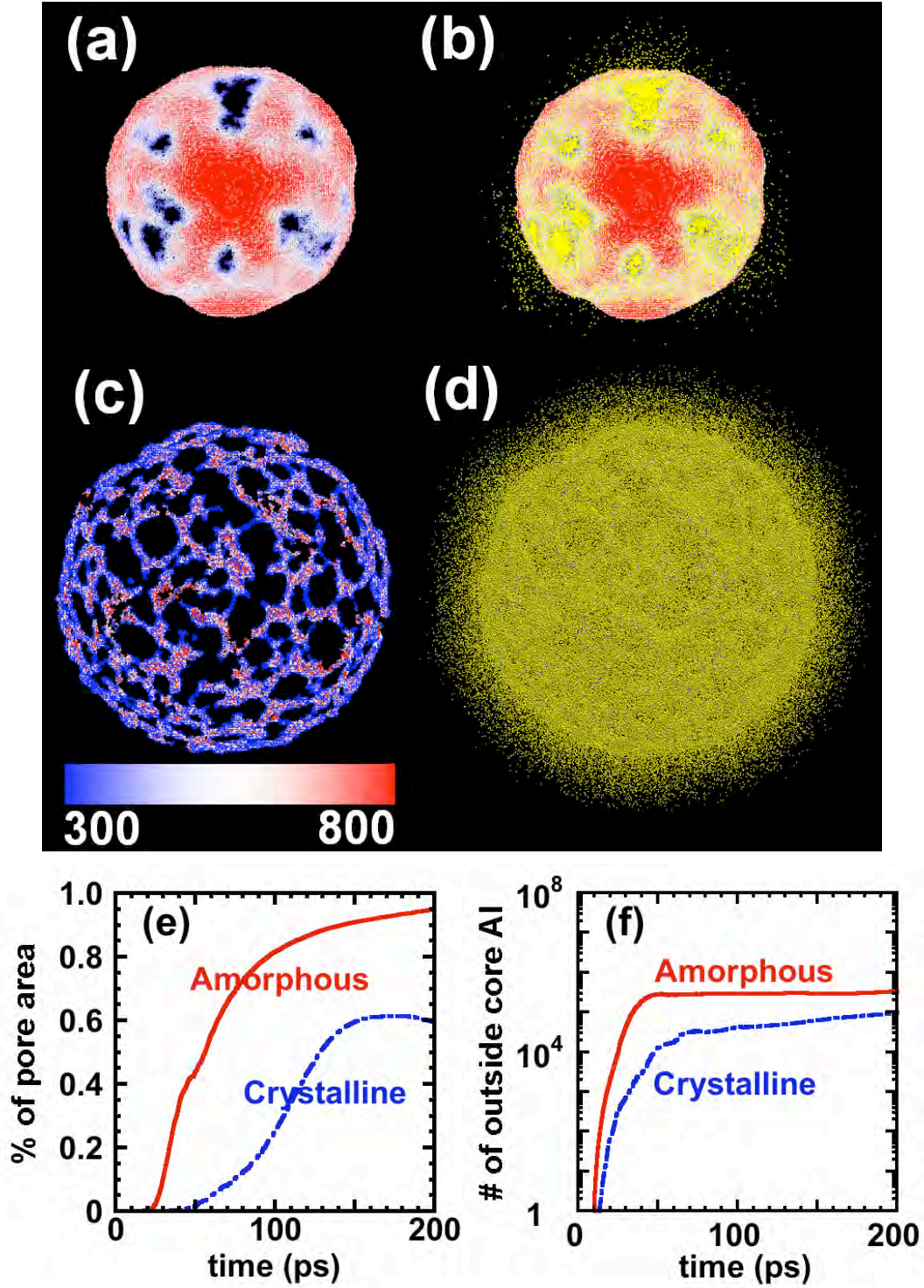


Fig. 6: (a) and (c) are snapshots of shell morphology in the CS and the AS systems, respectively, at 100 ps with the color representing the number density in the shell as shown by the color bar (in unit of # of atom/nm³). (b) and (d) are snapshots of the shell morphology combined with core aluminum atoms (yellow) for the two systems. (e) Percentage of the area of pores to that of the total shell; (f) Semi-log plot of the number of Al core atoms jetting into the environment in both systems.

Burning of Aluminum Nanoparticle by Slow Heating

The detonation of ANPs is a complex phenomena, which result from the interaction of several mechanisms taking place on scales ranging from the atomic interactions of individual chemically-reacting atoms (\sim angstroms) to the feature size of the total particle (5-10 nanometers). In the small scale, the creation of hotspots and the oxidation of spallated fragments contribute to the initiation and detonation phases of the reaction. On the larger scales, the mechanical breaking of the shell, phase changes within the component materials, and internal pressures which develop throughout the detonation also are expected to contribute to the overall behavior. As the overall evolution of the particle itself is a combination of these mechanisms, it is impossible to gain a comprehensive view of the controlling factors of detonation without being able to look at both scales simultaneously. To this end, we performed a multi-million atom MD simulations, which studied a particle being heated to a more conventional temperature (just above the melting point of aluminum) to accomplish the following objectives:

- (1) Analyze the burning of ANPs in order to better understand the mechanisms, which control its evolution.
- (2) Identify the key components of the initiation and burning of the ANP that need to be included in any coarser simulations that seek to properly capture its behavior on a larger scale.
- (3) Provide a contrast study to the laser-initiated simulation results, allowing comparison of the two initiation methods.

Several mechanisms leading to initiation in ANP materials have been presented in the scientific literature over the last decade. One predominant mechanism proposed by Pantoya, Levitas et al. for burning is that the particle remains stable until the core temperature exceeds the melting temperature of bulk aluminum ($T_m = 933$ K). At this point, the phase change from solid to liquid in the core (with the associated 12% volume increase) results in a considerable pressure buildup on the inner boundary of the shell. This pressure is enough to mechanically fracture the shell barrier, resulting in the spallation of unoxidized aluminum clusters into the surrounding oxidizer. The direct oxidation of these clusters is said to generate a large temperature increase, resulting in the complete burning of the particle and surrounding material.

From our simulations, we found the oxidation of the ANP due to heat-initiation to conventional temperature occurs in three phases. After the onset of reactions, the first stage is a confined heating during which the oxygen migrates from the shell into the core, releasing local heat. The second stage begins when the local temperature of the alumina shell exceeds the melting point of alumina, and results in shape deformation and an increase in oxygen absorption from the environment. Finally, during the third stage Al atoms are ejected from the surface of the shell and are directly oxidized by the surrounding oxygen. Detailed results, analysis, and interpretation of the MD simulation are shown below in order to understand fully the three phases we observed in our simulations.

The system simulated is a 46nm ANP with an amorphous alumina shell thermalized first at $T < 300$ K and then heated (100K/10ps) to 1200 K. After heating, the aluminum nanoparticle system is allowed to oxidize in an NVE (microcanonical) simulation for 1 ns (with a time step size of 1 fs). A center slice of the particle is visualized as shown throughout its evolution in Fig 7. In these images, the atoms initially part of the core region have been hidden to show the migration of oxygen atoms into the core region. The images show three trends, which will be explored with subsequent analysis:

- (1) The initial generation of heat at the core-shell boundary due to oxygen migration (0-60 ps).
- (2) Melting of the alumina shell (at ~50-60ps) resulting in shape deformation and increased uptake of oxygen (~50-80ps).
- (3) Ejection of small aluminum clusters into the surrounding oxygen gas, resulting in direct oxidation and additional heating (starting at ~80ps and continuing to simulation end).

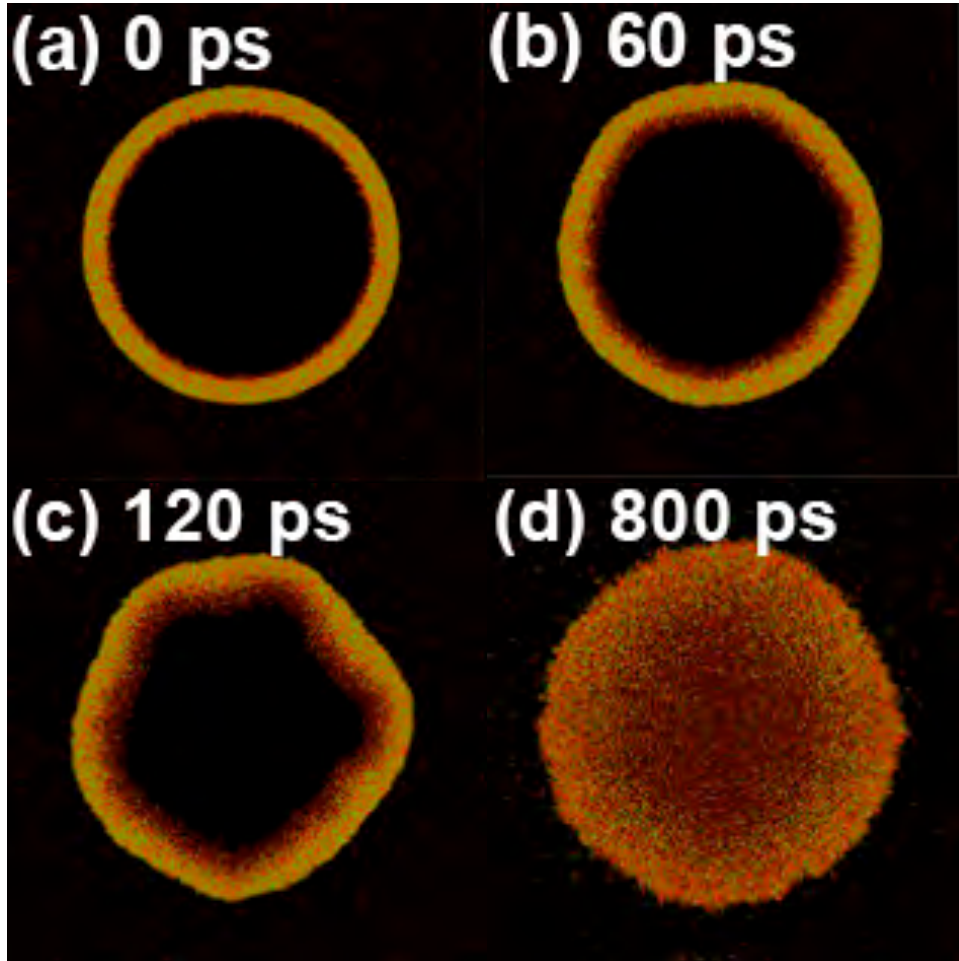


Fig 7: Snapshots of Center Slice of ANP with Core Al Atoms Hidden at time (a) 0, (b) 60, (c) 120 and (d) 800 ps.

The system temperature over time (Fig 8a) provides an insight into when the various mechanisms begin. As each mechanism results in a change in the rate of oxidative reactions in the particle, each causes a change in the amount of heat generated by the particle. Thus, the slope of the system's temperature provides an insight into when the changes in the controlling mechanisms occur. Once these turning points are identified, further analysis techniques may be employed to provide an insight into the details of these mechanisms.

In Fig 8b, three turning points are identified which indicate a change in the mechanism of oxidation. The first stage (from 0-50 ps), is defined by a large rate, which falls off quickly over time. At 50 ps, a turning point in the rate of heat generation points to the onset of a new mechanism, resulting in an increase in the rate of heat production. This time period, stage 2, continues until the next turning point at 100ps. After this time (throughout stage 3) the rate of heat generation decreases until the end of the simulation. With this 3 stage framework, we may

structure our analysis determine the mechanisms at play in the onset and continuation of each stage.

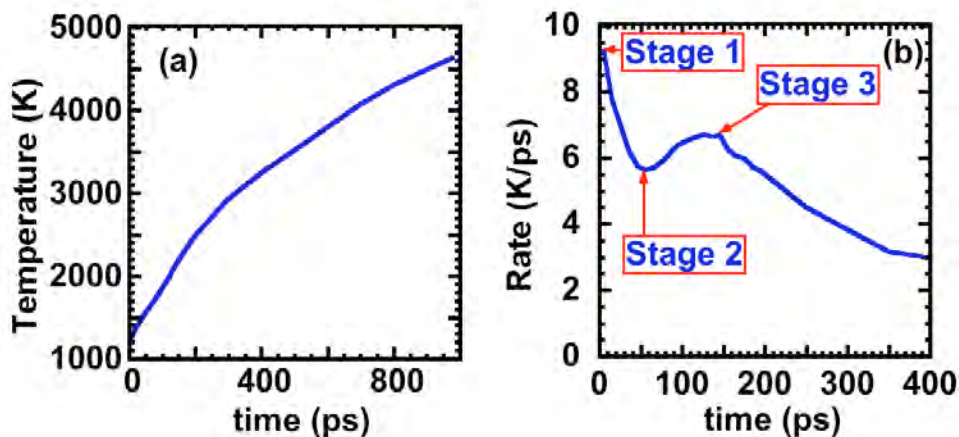


Fig 8: (a) Global temperature of system during NVE Simulation. (b) Rate of heat generated by system for the first 500ps.

Stage 1 – Initial Heat Generation due to Core-Shell Oxidation

The first 50 ps of the particle oxidation are dominated by reactions occurring at the core-shell boundary. The radial temperature graph during this time period shows a peak in the local temperature at the core-shell. This temperature can be linked to increased Al+O reactions as the oxygen migrates from the shell region into the core. This migration is also seen in an increase in aluminum-rich fragments and a decrease in the inner radius of the shell during this time period.

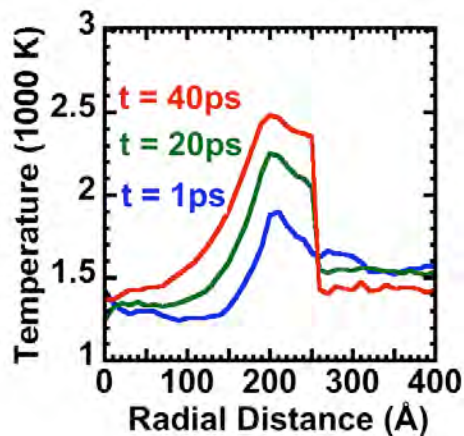


Fig 9: Radial temperature profile of ANP during stage 1 reaction.

Stage 2 – Shell Transformation and External Oxidation

At approximately 50 ps, the local temperature of the shell exceeds the melting temperature of bulk alumina ($T_m = 2330\text{K}$). Abruptly, a large change is detected in the outer radius of the particle, Fig. 10, as well as the loss of spherical symmetry in the particle shape (Fig 7 (b)-(c)). Subsequent to this change, the rate of heat generation in the total system begins to increase, as well as a local increase in temperature at the exterior boundary of the particle (Fig 9). The number of oxygen atoms in the shell sharply increases over this time period, indicating that the

molten alumina has greatly increased the absorption rate of the surrounding oxygen onto the particle.

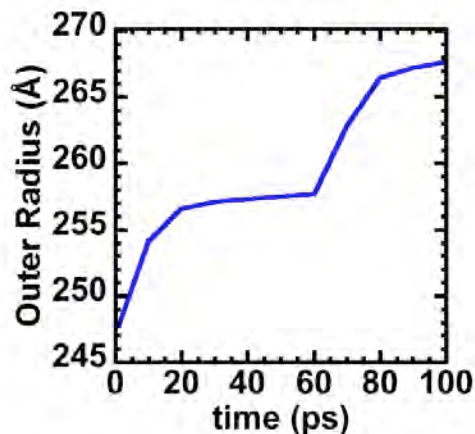


Fig 10: Change in outer radius of particle during the onset of stage 2 reaction.

Stage 3 – Al Cluster Ejections and Direct Oxidation of Fragments

At 80-90ps, a third change is detected in the mechanisms controlling particle oxidation, seen in the turning point in Fig. 8 (b). This is associated with the sudden increase of ejected aluminum atoms from the shell into the surrounding environment (Fig 11). The ejected aluminum atoms react with the surrounding oxygen by direct oxidation, resulting in a corresponding increase in oxygen-rich clusters (Fig 12). Finally, the presence of ejected aluminum atoms can be seen in the snapshots of Figs. 7 (c)-(d).

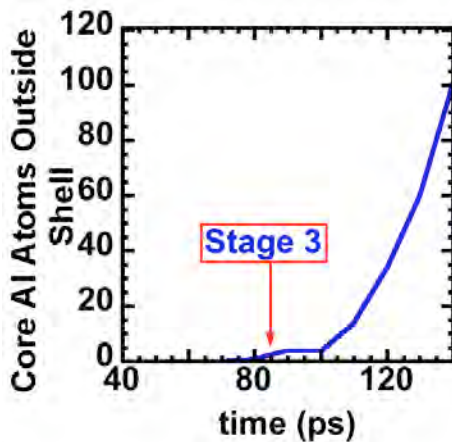


Fig 11: Al ejections in exterior during the onset of stage 3 reaction.

Examination of the original placement of the ejected atoms reveals that the shell Al atoms are seen in the exterior ~50 ps before the core Al atoms (100 ps vs. 150 ps). Also, the minimum shell thickness does not decrease below 20 Å during stage 2 and 3. Taken together, these results indicate that the ejected Al atoms are “baked off” the surface of the ANP shell, rather than escaping from the core through pores in the shell (as was the case in flash-heating simulations).

The above analysis demonstrates the importance of the inner core-shell boundary in the burning of the ANP. Unlike the laser-initiated detonation case (where the shell was fractured and ejected away from the particle upon initiation), in the heating case the shell has plenty of

time to greatly contribute to the burning process. This leads us to the conclusion that the core and the shell cannot be treated as two isolated pieces which interact only via the internal pressure. Instead, they must be considered as a chemically reacting combination.

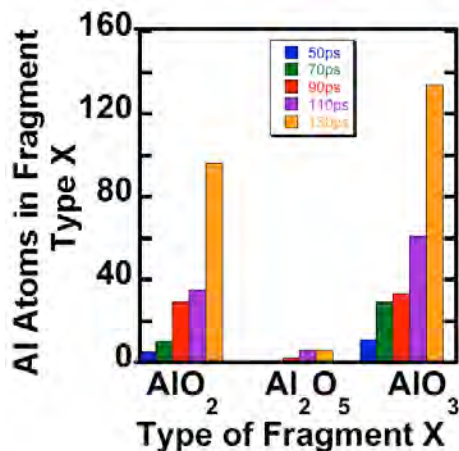


Fig 12: Increasing of Al atoms inside each type of fragments along with time.

Induced Synergetic Reactions of Multiple Aluminum Nanoparticles

To study the heat transport and oxidation reaction of ANP induced by neighboring ignited ANPs, we have performed multimillion atom MD simulation of the reaction dynamics of three ANPs on a linear chain. A system of three ANPs was created. Each ANP consisted of an aluminum core, 40 nm in diameter and a 3 nm amorphous alumina shell. Three such ANPs were placed 0.5 nm apart along a line. This system was then inserted into an environment of atomic oxygen. The MD box was of size $1938.4 \times 969.2 \times 969.2$ Å. Each ANP contained 1,973,159 atoms in the Al-core, 85,6475 Al atoms and 1,284,281 O atoms in the alumina shell. The background oxygen had 1,888,193 atoms. The entire system had 14,229,938 atoms. The outer ANPs (left and right) were slowly heated to a temperature of 1400 K using velocity scaling, while the central ANP and the background oxygen were kept at 500 K. After that, the system was left to react in NVE ensemble for 1 ns.

The hot outer (left and right) ANPs undergo self-sustained exothermic thermite reactions between Al and O atoms, resulting in continuous generation of heat inside the particles. The alumina shell in the outer ANPs melts at around 100 ps. Aluminum from the core of the outer ANPs begin to eject out of the shell at around 300 ps and the ANPs completely detonate by 600 ps. The central ANP, on the other hand, does not receive considerable heat till 300 ps, when the outer ANPs start to penetrate into the central ANP. The alumina shell of the central ANP melts at 500 ps and ejections from inside the aluminum core begin at 600 ps. In the initial stages, the primary mode of heat transfer from outer ANPs to the central ANP is convection. At 300 ps, the outer ANPs begin to penetrate into the central ANP. As evident from Fig. 13, the penetration begins through the respective zones of contact between the outer and the central ANPs, progressing gradually. After 1 ns of simulation, the three ANPs fuse together and form an ellipsoid.

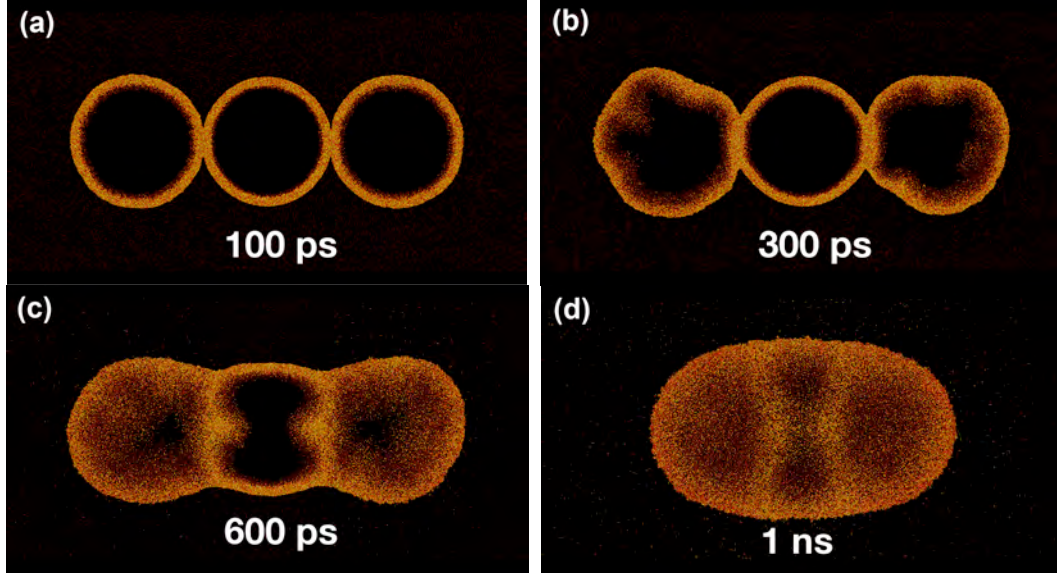


Fig. 13: Snapshots of the system at different stages of simulation. The outer (left and right) ANPs undergo detonation after being heated while the central ANP remains unaffected in the initial 300 ps. At ~300 ps the outer ANPs begin to penetrate the central ANP through the zones of contact, thus initiating burning and eventual detonation of the central ANP.

The outer ANPs behave in a similar fashion as observed in the study of isothermal heating of a single 46 nm ANP. To understand the burn rate, we need to look at the temperature gradient curves, which clearly show distinct stages in the overall burning process. The outer ANPs show three stages of burning (Fig. 14(a)), marked by the inflexion points, which is consistent with the previous study of burning of a single ANP. The onset of stage II in the outer ANPs occurs when the alumina shell melts (~2300 K). The central ANP, on the other hand, shows only two stages of burning (Fig. 14(b)). In the first stage, the temperature gradient increases till 600 ps. This is a combined effect of the penetration of hot particles from outer ANPs into the central ANP and the heat generated due to the reaction among the resident atoms.

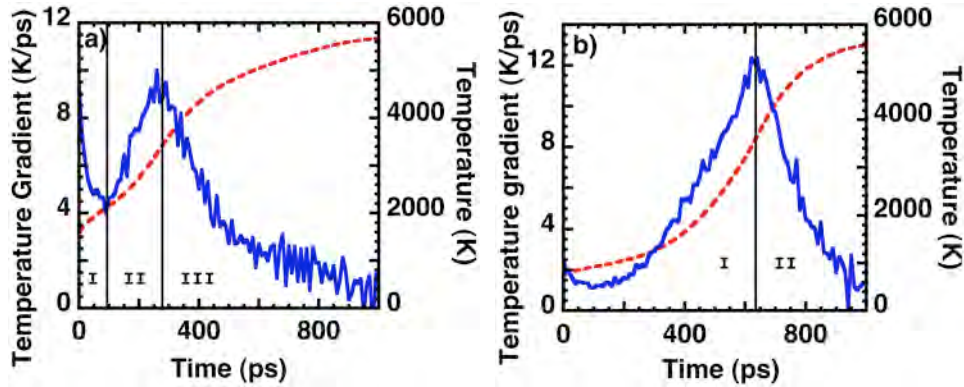


Fig. 14: Variation of Temperature and its gradient in outer (Fig. a) and central (Fig. b) ANPs. Temperature is shown as red dotted curve and the gradient is represented by blue solid curve. The outer and central ANPs undergo different stages of burning. The outer ANPs show three distinct stage of burning as observed in the case of isothermal heating of a single 46nm ANP. The central ANP, however, shows only two stages of burning. The onset of the last stage of burning in each ANP coincides with the beginning of ejections of pure Al atoms from the core to outside the shell.

The onset of the last stage of burning (stage III in outer ANPs and stage II in central ANP) coincides with the beginning of ejections from the respective Al-core (Fig. 15(a)). This suggests that at this point, the alumina shell develops perforations, resulting in Al atoms from the core jetting out in small clusters. This would result in release of internal stress within the ANPs, leading to a decline in the respective temperature gradient. As discussed earlier, the inflexion points in the temperature gradient curve correspond to different physical processes. The central ANP gets heated only when the hot particles from outer ANPs penetrate into it. This implies that in the initial period, the mode of heat transfer is convection. Penetration into the central ANP is evident when the number of atoms from outer ANPs present inside the central ANP is plotted against the distance from the center of the central ANP (Fig. 15(b)). As one can see, there is very less penetration into the central ANP in the first 200 ps. After 400 ps, the outer atoms are still close to the alumina shell. But by 600 ps, the outer atoms have penetrated half the radius of the central ANP and by 1 ns, the outer atoms can be seen to be present at the core. The average penetration front speed of the was estimated to be 54m/s.

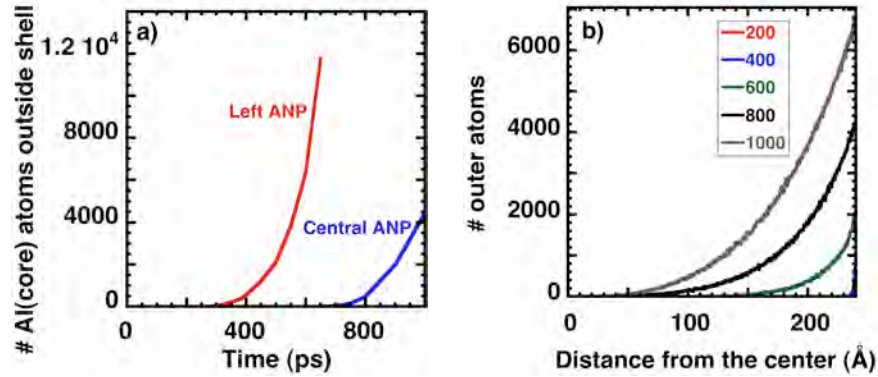


Fig. 15: (a) Ejection of pure Al atoms from the core to outside the shell. The outer ANPs (only the left one is shown here) begin ejecting out Al atoms from the core at ~300 ps while ejections in the central ANP begin at ~650 ps. (b) Penetration of atoms from outer ANPs into the central ANP after 200, 400, 600, 800 ps and 1ns of simulation. Outer atoms are not observed inside the central ANP in the first 300 ps. At 400 ps, the outer atoms can be seen inside the shell, though close to the shell-core interface. By 600 ps, the outer atoms have penetrated about half the radius of the central ANP and by 800 ps, they have reached the center of the core.

From the linear temperature profile of the system (Fig. 16), it is clear that the central ANP does not gain considerable heat in the initial 400 ps but in the next 400 ps, it attains almost the same temperature as the outer ANPs. By 1 ns, all the three ANPs attain a temperature of ~5500K and fuse together to form a single particle, ellipsoidal in shape. It can also be seen that the core of the central ANP is the last area to get heated, confirming the assertion that it is gaining heat due to convective heat transfer from the zones of contact, at least during the initial 600 ps.

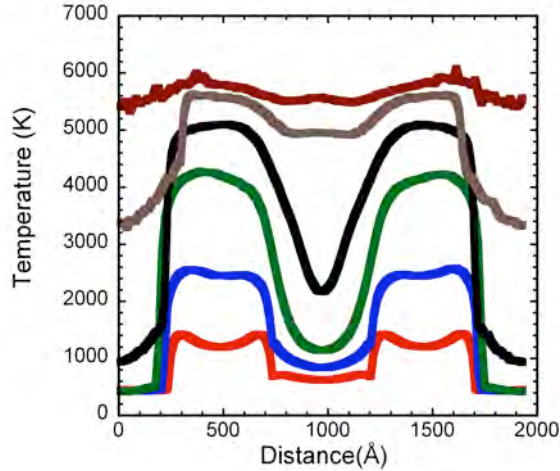


Fig. 16: Linear Temperature profile of the system. The local temperature is plotted against x-component of the distance from the origin. The lowermost curve represents the system just after heating and the subsequent curves represent the system after 200, 400, 600, 800 ps and 1 ns of simulation respectively. The outer ANPs were heated to 1400 K as evident from the graph. The temperature of the central ANP increases as heat flows into it from the outer ANPs through the zones of contact. Finally, all the three ANPs fuse together to form an ellipsoidal aggregate at an average temperature of 5500 K

Enhanced Reactivity of Nanothermite

We have performed DC-DFT MD simulations for a stack of Al and Fe_2O_3 layers involving 1152 (144 Fe_2O_3 + 432 Al) atoms in an orthorhombic supercell with dimensions (L_x, L_y, L_z) = (20.1 Å, 26.2 Å, 28.2 Å) with periodic boundary conditions. The hematite (Fe_2O_3) crystal, cut along (0001) planes to expose Fe planes, is placed in the supercell with the (0001) direction parallel to the z direction. The Fe planes of the hematite are attached to (111) planes of the face-centered cubic Al crystal at the two interfaces. Our DC-DFT method iteratively minimizes the energy functional using a preconditioned conjugate-gradient method to determine electronic wave functions. The grid spacing ~ 0.25 Å (corresponding to the cutoff energy of 45 Ry in the plane wave-based method) for the real-space representation of the wave functions is sufficiently small to obtain a good convergence of the total energy. We use a norm-conserving pseudopotentials and a generalized gradient approximation²² for the exchange-correlation energy. The DC-DFT method divides the system into 960 (= $8 \times 10 \times 12$) domains of dimensions $2.51 \times 2.62 \times 2.35$ Å. Figure 10 shows the side (yz) view of the non-overlapping cores of the domains in the supercell. Each domain is augmented with a buffer layer of depth ~ 2.2 Å to avoid boundary effects. The interatomic forces thus computed quantum-mechanically are used to integrate Newton's equations of motion numerically (with a time step of 0.84 fs) in MD simulations to study atomic motions and chemical reactions. The MD simulations are carried out at temperature 2000 K in the canonical ensemble.

Snapshots of the atomic configuration are shown in Fig. 17, where the side (yz) views of atomic configuration are displayed. We observe that the oxygen atoms in hematite migrate into the aluminum metal to form aluminum oxide and leaves behind liquid iron. Our DC-DFT simulation thus describes complete thermite reaction, $2\text{Al} + \text{Fe}_2\text{O}_3 \rightarrow \text{Al}_2\text{O}_3 + 2\text{Fe}$.

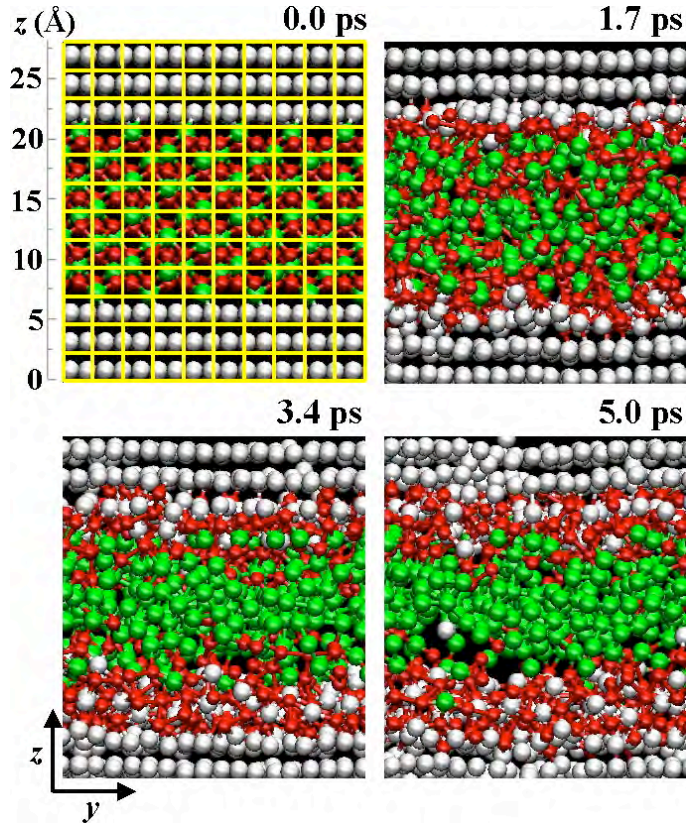


Fig. 17: Snapshots of the atomic configuration. The green, red and grey spheres show the positions of Fe, O and Al atoms, respectively. Yellow meshes at time 0 ps show the non-overlapping cores used by the DC-DFT method. Two interfacial regions are defined as slabs with a thickness of 4 Å parallel to the xy plane (length scale in angstrom is marked in the z direction). The Al- and Fe-side regions are defined between the two interfacial regions as shown in the figure.

To study mass diffusivity, Fig. 18 shows mean square displacements of O atoms along the z direction, which are calculated using the simulation data for 0-3 ps. The solid and dashed lines are obtained from O atoms in the interfacial and Fe-side regions, respectively. Here, the boundary between iron oxide and aluminum oxide at each interface is located by calculating the average z coordinate of Al atoms facing Fe atoms. The interfacial regions are then defined as slabs with a thickness of 4 Å (i.e. 2 Å above and below the boundaries) parallel to the xy plane as shown in Fig. 17. Figure 18 shows that O atoms in the interfacial region are much more diffusive than those on the Fe side. The four-fold accelerated diffusion constant perpendicular to the interface is $2 \times 10^{-4} \text{ cm}^2/\text{s}$ in the interfacial region.

To understand the mechanism of the enhanced diffusivity at the interface, we have examined the time evolution of the atomic configuration in the interfacial region and found a concerted metal-oxygen flip mechanism. That is, O atoms switch their positions with neighboring Al atoms while diffusing in the z direction. A typical example of such events is shown in Fig. 19, where the middle panel shows the time evolution of the z coordinates of the O and Al atoms of interest. The O atom moves upward in concert with the Al atom moving downward. The switching motion between the O and Al atoms is shown in the bottom panel of Fig. 19.

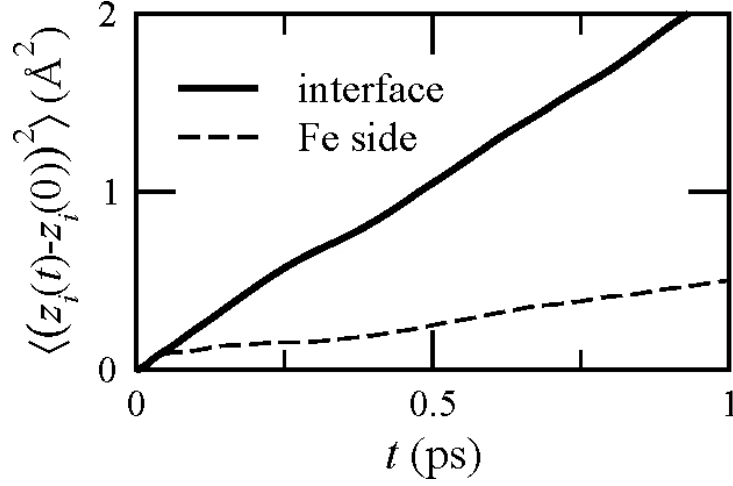


Fig. 18: Enhanced diffusion at the metal-oxide interface. Mean square displacements of O atoms along the z direction are plotted as a function of time. The solid and dashed curves are for O atoms in the interfacial and Fe-side regions, respectively.

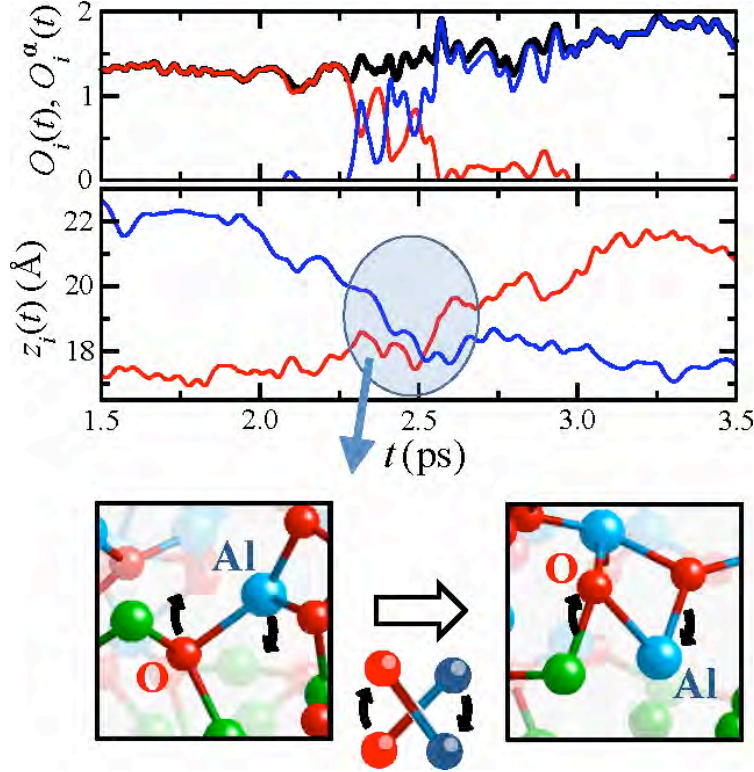


Fig. 19: Concerted metal-oxygen flip mechanism. (Top panel) Time evolution of the total and partial SBOP, $O_i(t)$ and $O_i^\alpha(t)$, associated with the oxygen atom labeled as 'O' in the bottom panel. The black, red and blue curves show $O_i(t)$, $O_i^{\text{Fe}}(t)$ and $O_i^{\text{Al}}(t)$, respectively. (Middle panel) Time evolution of the z coordinates of the O and Al atoms labeled as 'O' and 'Al' in the bottom panel, respectively. (Bottom panel) Atomic configurations near the O and Al atoms of interest (labeled as 'O' and 'Al') at 2.3 and 2.8 ps. The green, red and blue spheres are Fe, O and Al atoms, respectively.

To explain the quantum-mechanical origin of this mechanism, we calculate the bond-overlap population $O_{ij}(t)$ between i^{th} and j^{th} atoms as a function of time t . We also define the sum of the bond-overlap population (SBOP) for each oxygen atom: Partial SBOP $O_i^\alpha(t)$ for the i^{th} oxygen

atom is defined as $O_i^\alpha(t) = \sum_{j \in \alpha} O_{ij}(t)$, where α is Fe or Al; and the total SBOP is $O_i(t) = O_i^{\text{Fe}}(t) + O_i^{\text{Al}}(t)$. The upper panel of Fig. 19 shows $O_i(t)$ and $O_i^\alpha(t)$ associated with the O atom. For $t < 2.3$ ps, the oxygen atom resides in the iron-oxide region, and $O_i^{\text{Fe}}(t)$ has finite values, while $O_i^{\text{Al}}(t)$ is nearly zero. At $t \sim 2.3$ ps, the oxygen atom starts to migrate into the aluminum side and $O_i^{\text{Al}}(t)$ begins to increase. For $2.3 \text{ ps} < t < 2.7 \text{ ps}$, $O_i^{\text{Fe}}(t)$ and $O_i^{\text{Al}}(t)$ have comparable values while the oxygen atom is moving across the interface. For $t > 3.0$ ps, $O_i^{\text{Fe}}(t)$ becomes zero, while $O_i^{\text{Al}}(t)$ converges to a finite value, indicating that the oxygen atom is chemically bonded only with Al atoms. The switching motion between O and Al atoms at the interface is thus triggered by the change of chemical bonding associated with these atoms.

To quantify the collective switching motion between O and Al atoms, we calculate the correlation function between the displacements of atoms along the z direction:

$$d_{\text{O-Al}}(t) = \langle \Delta z_i(t) \cdot \Delta z_j(t) \rangle / t^2, \quad (1)$$

where $\Delta z_i(t) = z_i(t+t_0) - z_i(t_0)$ with $z_i(t)$ being the z coordinate of the i^{th} ion at time t . The brackets mean the average over both the time origin t_0 and atomic pairs ($i \in \text{O}, j \in \text{Al}$). In the calculation, atomic pairs whose distance is less than 2.3 \AA at t_0 are selected. Since we are interested in the correlation between diffusing O and Al atoms, we include atomic pairs that satisfy the conditions $|\Delta z_i(t)| > 2 \text{ \AA}$ and $|\Delta z_j(t)| > 2 \text{ \AA}$ at $t = 2 \text{ ps}$. The results in Fig. 20(a) (solid curve) reveal negative correlation in $d_{\text{O-Al}}(t)$ for $t > 0.5 \text{ ps}$, which reflects the collective switching motion between O and Al atoms at the interface as shown in Fig. 19. Such negative correlation does not exist on the Al side (see the dashed curve in Fig. 20(a)), indicating independent diffusive motions of Al and O atoms.

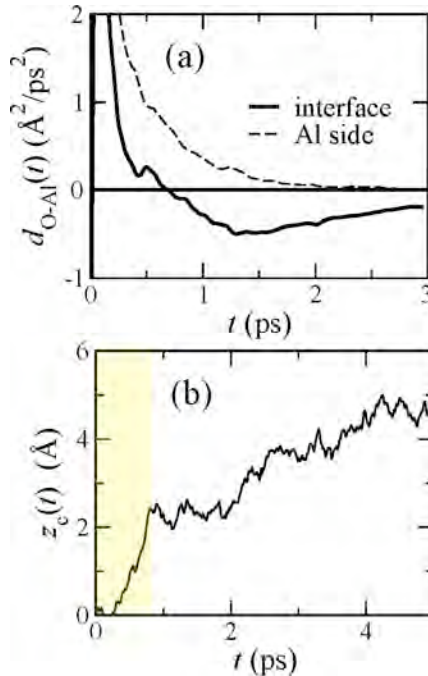


Fig. 20: (a) Negative correlation associated with concerted Al and O motions at the interface. Correlation functions between displacements of O and Al atoms along the z direction (defined in Eq. (1)) are shown as a function of time. The solid and dashed curves are obtained in the interfacial and Al-side regions. (b) Two-stage reactions of thermite. Time evolution of the positions $z_c(t)$ of the reaction fronts. The gray shade highlights the rapid first-stage reaction due to concerted Al-O motions, which is followed by slow reaction based on uncorrelated diffusion.

The enhanced mass diffusivity at the metal-oxide interface leads to a two-stage reaction behavior. In Fig. 20(b), we plot the position $z_c(t)$ of the reaction front calculated from the coordinates of oxygen atoms at the forefront of oxidation. For $t < 1$ ps, $z_c(t)$ increases rapidly as oxygen atoms migrate into the Al side, which is accelerated by the collective switching mechanism. This is followed by a slower reaction due to uncorrelated diffusion of atoms. (Though slower than the concerted thermite reaction, the second-stage diffusion here could still be faster than conventional diffusion, due to defect-mediated giant diffusivity because of the depletion of O atoms in the near-interface oxides.) Such two-stage reactions may be related to the experimental observation in thermite nanowire arrays mentioned before.

Personnel Supported/Associated:

- Faculty (Rajiv K. Kalia, Aiichiro Nakano, Priya Vashishta)
- Visiting faculty (Fuyuki Shimojo)
- Graduate students (Richard Clark, Ken-ichi Nomura, Richard Seymour, Weiqiang Wang)

Publications:

1. "Multimillion atom reactive simulations of nanostructured energetic materials," P. Vashishta, R. K. Kalia, A. Nakano, B. E. Homan, and K. L. McNesby, *Journal of Propulsion and Power* **23**, 688-692 (2007).
2. "1,3,5-trinitro-1,3,5-triazine decomposition and chemisorption on Al(111) surface: first-principles molecular dynamics study," N. Umezawa, R. K. Kalia, A. Nakano, P. Vashishta, and F. Shimojo, *Journal of Chemical Physics* **126**, 234702: 1-7 (2007).
3. "A divide-and-conquer/cellular-decomposition framework for million-to-billion atom simulations of chemical reactions," A. Nakano, R. K. Kalia, K. Nomura, A. Sharma, P. Vashishta, F. Shimojo, A. C. T. van Duin, W. A. Goddard, III, R. Biswas, and D. Srivastava, *Computational Materials Science* **38**, 642-652 (2007).
4. "Dynamic transition in the structure of an energetic crystal during chemical reactions at shock front prior to detonation," K. Nomura, R. K. Kalia, A. Nakano, P. Vashishta, A. C. T. van Duin, and W. A. Goddard III, *Physical Review Letters* **99**, 148303: 1-4 (2007).
5. "Reactive nanojets: nanostructure-enhanced chemical reactions in a defected energetic crystal," K. Nomura, R. K. Kalia, A. Nakano, and P. Vashishta, *Applied Physics Letters* **91**, 183109: 1-3 (2007).
6. "Fracture initiation mechanisms in α -alumina under hypervelocity impact," C. Zhang, R. K. Kalia, A. Nakano, and P. Vashishta, *Applied Physics Letters* **91**, 121911: 1-3 (2007).
7. "Electronic processes in fast thermite reaction: a first-principles molecular dynamics study," F. Shimojo, A. Nakano, R. K. Kalia, and P. Vashishta, *Physical Review E* **77**, 066103: 1-7 (2008).
8. "Deformations and failure of α -alumina under hypervelocity impact loading," C. Zhang, P. S. Branicio, R. K. Kalia, A. Nakano, and P. Vashishta, *Journal of Applied Physics* **103**, 083508: 1-15 (2008).
9. "Atomistic damage mechanisms during hypervelocity projectile impact on AlN: a large-scale parallel molecular dynamics simulation study," P. S. Branicio, R. K. Kalia, A. Nakano, P.

- Vashishta, F. Shimojoc, and J. P. Rino, *Journal of the Mechanics and Physics of Solids* **56**, 1955-1988 (2008).
10. "Interaction potentials for alumina and molecular dynamics simulations of amorphous and liquid alumina," P. Vashishta, R. K. Kalia, A. Nakano, and J. P. Rino, *Journal of Applied Physics* **103**, 083504: 1-13 (2008).
 11. "A scalable parallel algorithm for large-scale reactive force-field molecular dynamics simulations," K. Nomura, R. K. Kalia, A. Nakano, and P. Vashishta, *Computer Physics Communications* **178**, 73-87 (2008).
 12. "Metascale molecular dynamics simulation of nano-mechano-chemistry," F. Shimojo, R. K. Kalia, A. Nakano, K. Nomura, and P. Vashishta, *Journal of Physics: Condensed Matter* **20**, 294204: 1-9 (2008).
 13. "De novo ultrascale atomistic simulations on high-end parallel supercomputers," A. Nakano, R. K. Kalia, K. Nomura, A. Sharma, P. Vashishta, F. Shimojo, A. C. T. van Duin, W. A. Goddard, III, R. Biswas, D. Srivastava, and L. H. Yang, *International Journal of High Performance Computing Applications* **22**, 113-128 (2008).
 14. "Divide-and-conquer density functional theory on hierarchical real-space grids: parallel implementation and applications," F. Shimojo, R. K. Kalia, A. Nakano, and P. Vashishta, *Physical Review B* **77**, 085103:1-12 (2008).
 15. "Fast reaction mechanism of a core (Al)-shell (Al_2O_3) nanoparticle in oxygen," W. Wang, R. Clark, A. Nakano, R. K. Kalia, P. Vashishta, *Applied Physics Letters* **95**, 261901 (2009).
 16. "Molecular dynamics nanoindentation simulation of an energetic materials," Y. Chen, K. Nomura, R. K. Kalia, A. Nakano, and P. Vashishta, *Applied Physics Letters* **103**, 035501 (2009).
 17. "Enhanced reactivity of nanoenergetic materials: a first-principles molecular dynamics study based on divide-and-conquer density functional theory," F. Shimojo, A. Nakano, R. K. Kalia, and P. Vashishta, *Applied Physics Letters* **95**, 043114 (2009).
 18. "A metascale computing framework for large spatiotemporal-scale atomistic simulations," K. Nomura, H. Dursun, R. Seymour, W. Wang, R. K. Kalia, A. Nakano, P. Vashishta, F. Shimojo, and L. H. Yang, in *Proceedings of the International Parallel and Distributed Processing Symposium* (IEEE, Rome, Italy, 2009).
 19. "Multi-million atoms molecular dynamics study of combustion mechanism of aluminum nanoparticle," W. Wang, R. Clark, A. Nakano, R. K. Kalia, P. Vashishta, *Materials Research Society Symposium Proceedings* **1137**, EE-10-29 (2009).
 20. "Density functional study of 1,3,5-trinitro-1,3,5-triazine molecular crystal with van der Waals interactions," F. Shimojo, Z. Wu, A. Nakano, R. K. Kalia, and P. Vashishta, *Journal of Chemical Physics*, in press (2010).

Interactions:

1. "Multimillion atom simulations of nanostructured materials", International Symposium on "Theory of Atomic and Molecular Clusters, TAMC5", Richmond, VA (May 16, 2007)

2. "March Toward Petaflops: High Performance Computing and Research and Education in Computational Science and Engineering", University of Pittsburgh, Pittsburgh, PA, (March 25, 2007)
3. "Multimillion to billion atom simulations of nanostructured materials under extreme conditions", Multi-Scale and Large-Scale Simulation in DoD Materials Science, Mitre Corporation, McLean, VA, (June 14-15, 2007)
4. "Billion-atom simulation of mechanochemical processes on world's fastest supercomputers," *Okayama University* (June 27, 2007, Okayama, Japan)
5. "Multimillion atom simulations of nanorods, dynamics of wing cracks, hypervelocity impact damage, and planar shock on RDX", Symposium on Bold Predictions in Theoretical Chemistry: A Symposium in Honor of One of the Boldest, Bill Goddard, on the Occasion of his 70th Birthday, American Chemical Society, Boston, MA, (August 19-23, 2007)
6. "Peta-scalable reactive molecular dynamics simulation of mechanochemical processes," CECAM (Centre Européen de Calcul Atomique et Moléculaire) Workshop on Linear-Scaling Ab Initio Calculations: Applications and Future Directions (September 3, 2007, Lyon, France).
7. "Multimillion to billion atom simulations of nanostructured materials," 17th IKETANI International Conference on Dreams, Creation and Realization of Materials Saving the Humankind (September 5-8, 2007, Tokyo, Japan).
8. "Metascaleable molecular dynamics simulation of mechanochemical processes," Third International Workshop on High-Performance Computing for Nano-science and Technology (November 16, 2007, Reno, NV).
9. "Multimillion to billion atom simulations of nanostructured materials under extreme conditions," Symposium on Ultrascale Hierarchical Simulations on High-End Parallel and Distributed Computers (December 3-6, 2007, Kyoto, Japan).
10. "Metascaleable reactive atomistic simulation of nano-mechano-chemistry," International Workshop on Large-scale Matrix Computation and Applications in Physics and Engineering Science (December 13, 2007, Tokyo, Japan).
11. "Multimillion to billion atom simulations of reactive nanosystems," Workshop on Pseudopotentials and Complex Materials (April 10-11, 2008, Austin, TX).
12. "Multimillion to billion atom simulations of nanosystems under extreme conditions," The 21st Kronsberg Seminar on Fragmentation processes in the Earth (May 7-9, 2008, Kronsberg, Norway).
13. "Multimillion to billion atom simulations of nanoenergetic materials," DARPA Workshop on Microthermal Initiator and Nanoenergetics Device (May 22-23, 2008, Beltsville, MD).
14. "Large spatiotemporal-scale atomistic simulations of materials on petaflops computers," International Conference of the Grand Challenge to Next-Generation Integrated Nanoscience (June 6, 2008, Tokyo, Japan).
15. "Atomistic simulations on petascale machines," JEOM Colloquium (July 9-11, 2008, Seattle, WA).

16. "Multimillion-to-billion atom molecular dynamics simulations of deformation, flow, fracture and nanoindentation in silica glass," *International Conference on Theory and Applications of Computational Chemistry*, Shanghai, China, September 23-27, 2008.
17. Keynote lecture, *SES 2008 Meeting on Multiscale Modeling of Defects in Solids*, University of Illinois at Urbana Champaign, IL, October 12-15, 2008.
18. "A metascalable computing framework for large spatiotemporal-scale atomistic simulations," *Workshop on Computational Science Frontiers*, Nagoya, Japan, November 26, 2008.
19. "Multimillion to billion atom simulations of nanosystems under extreme conditions," *Computational Approaches and Applications in Earth Materials Studies*, American Geophysical Union, San Francisco, CA, December 15-19, 2008.
20. "Multibillion-atom simulations of nano-mechano-chemistry on petaflops computers," *First International Symposium on Global Center of Excellence for Mechanical Systems Innovation*, Tokyo, Japan, February 2, 2009.
21. "Large spatiotemporal-scale material simulations on petaflops computers (opening keynote)," *Winter School on Multiscale Simulation Methods in Molecular Sciences*, Jülich, Germany, March 2, 2009.
22. "High performance computing for billion atom simulations of nanosystems," *Scientific Discovery through Advanced Computing, ICCES'2009*, Phuket, Thailand, April 7-11, 2009.
23. "Petascale simulations of hard and soft condensed phase systems," University of California at Davis, April 30, 2009.
24. "Multimillion atom simulations of reactive nanosystems," *Symposium on Nano-scale Energetic Materials: Fabrication, Characterization and Molecular Modeling*, E-MRS, Strasbourg, France, June 8-12, 2009.
25. "Metascalable atomistic simulations of nano-mechano-chemistry on petaflops computers," *European Materials Research Society 2009 Spring Meeting*, Strasbourg, France, June 10, 2009.
26. "Multimillion to billion atom simulations of nanostructured materials under extreme conditions," *Symposium in Honor of Professor Sidney Yip, USNCCM 10*, Columbus, OH, July 16-18, 2009.
27. "Large reactive molecular dynamics simulations of nano-mechano-chemistry on petaflops computers," *Workshop on "Molecular Dynamics with Reactive Potentials"*, Memphis, TN, August 5, 2009.
28. "Reactive molecular dynamics simulations of nano-mechano-chemistry on petaflops computers," *Fourth Meeting on "Reactive Potential Development"*, Madison, WI, September 19, 2009.
29. "Petascalable molecular dynamics simulations of nano-mechano-chemistry," *Workshop on "Towards Microscale Molecular Simulations with High-Performance Computing"*, Dublin, Ireland, October 15, 2009.

Transitions:

The atomistic understanding gained in this project will lead to the development of new and improved materials and structures with enhanced energy density and reduced sensitivity for a wide range of DoD applications, by significantly accelerating the pace of experimental research and through our extensive collaborations with DoD scientists (Dr. William Wilson at DTRA; joint paper “multimillion atom reactive simulations of nanostructured energetic materials” in *Journal of Propulsion and Power* with Dr. Barrie Homan and Dr. Kevin McNesby at ARL; our students’ internships with Dr. Betsy Rice and Dr. Margaret Hurley at ARL; and mutual visits by Dr. Brad Forch and Dr. Shashi Karna at ARL). Our dual-degree students (Ph.D. in the physical sciences or engineering with MS in Computer Science specialized in High Performance Computing and Simulations) continue to do internships with our DoD collaborators.

**DISTRIBUTION LIST
DTRA-TR-14-46**

DEPARTMENT OF DEFENSE

DEFENSE THREAT REDUCTION
AGENCY
8725 JOHN J. KINGMAN ROAD
STOP 6201
FORT BELVOIR ,VA 22060
ATTN: S. PEIRIS

DEFENSE TECHNICAL
INFORMATION CENTER
8725 JOHN J. KINGMAN ROAD,
SUITE 0944
FT. BELVOIR, VA 22060-6201
ATTN: DTIC/OCA

**DEPARTMENT OF DEFENSE
CONTRACTORS**

QUANTERION SOLUTIONS, INC.
1680 TEXAS STREET, SE
KIRTLAND AFB, NM 87117-5669
ATTN: DTRIAC